

Low energy (e,2e) coincidence studies of NH₃: Results from experiment and theory

Kate L. Nixon, Andrew James Murray, Hari Chaluvadi, Chuangang Ning, James Colgan, and Don H. Madison

Citation: *The Journal of Chemical Physics* **138**, 174304 (2013); doi: 10.1063/1.4802960

View online: <http://dx.doi.org/10.1063/1.4802960>

View Table of Contents: <http://scitation.aip.org/content/aip/journal/jcp/138/17?ver=pdfcov>

Published by the [AIP Publishing](#)



Re-register for Table of Content Alerts

Create a profile.



Sign up today!



Low energy ($e,2e$) coincidence studies of NH_3 : Results from experiment and theory

Kate L. Nixon,¹ Andrew James Murray,¹ Hari Chaluvadi,² Chuangang Ning,³ James Colgan,⁴ and Don H. Madison²

¹Photon Science Institute, School of Physics and Astronomy, University of Manchester, Manchester M13 9PL, United Kingdom

²Department of Physics, Missouri University of Science and Technology, Rolla, Missouri 65409, USA

³Department of Physics, State Key Laboratory of Low-Dimensional Quantum Physics, Tsinghua University, Beijing 100084, China

⁴Theoretical Division, Los Alamos National Laboratory, Los Alamos, New Mexico 87545, USA

(Received 14 February 2013; accepted 11 April 2013; published online 3 May 2013)

Experimental and theoretical triple differential cross sections (TDCS) from ammonia are presented in the low energy regime with outgoing electron energies from 20 eV down to 1.5 eV. Ionization measurements from the $3a_1$, $1e_1$, and $2a_1$ molecular orbitals were taken in a coplanar geometry. Data from the $3a_1$ and $1e_1$ orbitals were also obtained in a perpendicular plane geometry. The data are compared to predictions from the distorted wave Born approximation and molecular-three-body distorted wave models. The cross sections for the $3a_1$ and $1e_1$ orbitals that have p -like character were found to be similar, and were different to that of the $2a_1$ orbital which has s -like character. These observations are not reproduced by theory, which predicts the structure of the TDCS for all orbitals should be similar. Comparisons are also made to results from experiment and theory for the iso-electronic targets neon and methane. © 2013 AIP Publishing LLC. [<http://dx.doi.org/10.1063/1.4802960>]

I. INTRODUCTION

The ionization of atoms and molecules by electron impact is important in many fundamental and applied areas. A full and detailed understanding of this process is, however, still incomplete. The technique of ($e,2e$) spectroscopy¹ provides the most comprehensive data from these electron impact ionization processes, since the experiments are kinematically complete. As such, sophisticated theoretical models describing these types of collision are most rigorously tested against ($e,2e$) data. Current state of the art models for atomic targets include relativistic and non-relativistic distorted wave Born approximations (DWBA),^{2,3} time dependant close coupling (TDCC)⁴ and convergent close coupling (CCC) theories,⁵ and R-matrix with pseudo-states models.⁶ These calculations now provide good agreement with experiment over a wide energy range for lighter targets. Only the TDCC and DWBA models have been applied to molecular targets, the TDCC model currently being restricted to hydrogen. New theories are hence required to predict the ionization of more complex molecules. Many of the current predictions are based upon the DWBA. The molecular three-body distorted wave approximation (M3DW)⁷ used in the present studies employs the Ward-Macek factor to include post-collision interactions. Alternatively, Champion *et al.*⁸ use three Coulomb waves to model the final state, often referred to as the BBK method. Toth and Nagy have developed a total screening model for their direct transition matrix elements.⁹

The challenges that occur for ionization models from molecular targets are considerable, as the electron collision gives rise to many additional complexities that need to be carefully considered. Most obvious of these is that the

nuclei are distributed throughout the molecule, which leads to a reduction in symmetry of the interaction compared to that for an atom. Given that the target molecules are also randomly aligned in almost all experimental studies, this presents a major challenge to any theory that wishes to directly compare to experiment. Additionally, since each atom within a molecule may act as a scattering centre, the collision dynamics are considerably more complex. Other properties unique to molecules include their internal rotational and vibrational degrees of freedom, which also may need to be considered. Many molecules have orbitals that are closely spaced in energy, and they may be liquids or solids under normal temperatures and pressures. These complexities can be addressed by careful choice of the target under consideration, and by employing molecular beam ovens to yield sufficient vapour pressure in the interaction region to allow accurate experimental data to be obtained.

Ammonia (NH_3) is an excellent target to study from both experimental and theoretical aspects. It is gaseous at room temperature and has three well-separated orbitals (with ionization potentials of ~ 11 , 16.74, and 27.74 eV),¹⁰ making measurements from individual states straightforward to conduct and analyze. Furthermore, since ammonia is a relatively simple molecule with only four atoms and ten electrons, this should aid in reducing the complexity of the theoretical computations.

Accurate wavefunctions for NH_3 are available using standard quantum chemical software packages, as established most recently by Zhu *et al.*¹¹ Calculations of the momentum distributions derived from these wavefunctions were compared to electron momentum spectroscopy (EMS) data to confirm their quality. It has also been shown recently that a

single centred molecular orbital can reproduce high-energy EMS data, suggesting that multi-centred wavefunctions may not be necessary in this high energy regime.¹²

Recent low energy or dynamical ($e,2e$) studies have highlighted the importance of electron-nuclei interactions in electron impact ionization collisions.^{13,14} These investigations show that spherical averaging of the nuclear frame can produce unrealistically low nuclear density for the atoms located away from the centre of mass (CM), i.e., the nuclear charge of such atoms is distributed on a sphere of radius equal to the distance between the CM and the nucleus. In turn, this results in theory underestimating the scattering from these nuclei in the molecule. Improvement in agreement between experiment and theory was seen by increasing the nuclear contribution to the distorting potential, achieved through a reduction of the radius of the equivalent sphere of charge. This method demonstrates that important physical processes are probably being masked by the spherical averaging process.

The aim of the present study is to evaluate the influence various parameters have on the scattering dynamics. Initially, the effect of the orbital character is assessed by comparing and contrasting the data from the two outermost orbitals of NH_3 , which both have p -like character. The results are then compared to data from the third outermost orbital that has s -like character. To assess the influence of the molecular structure, the data from NH_3 is then compared to results from the iso-electronic targets neon (Ne) and methane (CH_4). By studying neon, a comparison can be made between experimental and theoretical data without the added complexities introduced by a molecular target. This provides a baseline from which to assess the predictions for the different molecules. The M3DW model used for the molecules contains the same scattering physics as the model used for neon, but adopts a more complex molecular wavefunction for both the neutral molecule and ion. The model also includes a spherical averaging process to allow for the random orientation of the molecules in the experiment. Finally, by comparing data from both atomic and molecular species, the influence of the nuclear frame on the scattering process can be ascertained. This is possible since methane and ammonia have a similar frame, with the light H nuclei separated from the heavier atom, whereas neon has all of the nuclear charge located at a single point in space.

By systematically assessing the effect of these parameters on the ionization process, the strengths and weaknesses of the models can be determined. This will allow further improvement and refinement of the models to increase the accuracy of the predictions. A steady improvement of the early atomic interaction models was achieved through systematic and detailed comparison to experimental ($e,2e$) data. It is expected that such improvements will also accrue for these new theories describing interactions with molecular targets through a similar rigorous comparison to different species.

This paper is presented as follows. After this Introduction the structure and orbitals of ammonia are briefly discussed in Sec. II. Section III outlines key features of the ($e,2e$) spectrometer used to determine the triple differential cross sections (TDCS), and Sec. IV describes the models used to generate the predicted cross sections. Results from experiment and theory are compared in Sec. V. Data from coplanar

scattering are given in Sec. V A, and results from the perpendicular plane geometry are in Sec. V B. Conclusions from this work together with suggestions for future studies are in Sec. VI.

II. MOLECULAR STRUCTURE OF AMMONIA

Prior to considering electron impact ionization from NH_3 , it is useful to describe the molecular structure and introduce the orbital labeling conventions used in this paper. The structure of ammonia falls into the C_{3v} group, having a trigonal pyramidal geometry. The centre of mass (CM) for this molecule does not correspond to the position of the nitrogen atom. This has a bearing on the calculations that are presented below, which average the molecular structure over all orientations prior to modelling the collision. This averaging (as described in Sec. IV) is performed around the CM. For NH_3 this results in a nuclear charge structure consisting of two concentric thin spheres of charge: an *outer* sphere due to the hydrogen nuclei which is $\sim 2 \text{ \AA}$ in diameter and an *inner* spherical shell due to the nitrogen nucleus which is $\sim 0.13 \text{ \AA}$ in diameter. Since no nuclei reside at the centre of mass of the molecule, the interior of the inner spherical charge shell is then field-free. Electrons that enter this small region will therefore not be deflected.

Molecular orbital theory gives rise to three valence energy levels (see Figure 1). The highest energy level (or highest occupied molecular orbital, HOMO) is singly degenerate and has $3a_1$ symmetry, so it behaves according to the operations of the A_1 symmetry label within the character table for NH_3 .¹⁶ In these orbital configurations the “ a ” denotes it is a singly degenerate orbital, whereas the “ e ” denotes a doubly degenerate orbital. The subscript “1” indicates the orbital is symmetric with reflection through a σ_v mirror plane (i.e., vertical through the N and H and dissecting the H–N–H bond angle), whereas the leading number “3” indicates it is the 3rd orbital of this type in the molecule.

The $3a_1$ orbital is a non-bonding orbital and is attributed to the lone pair of electrons on the nitrogen atom. Both electron momentum spectroscopy measurements^{11,17} and *ab initio*¹¹ calculations show it has dominant p -like

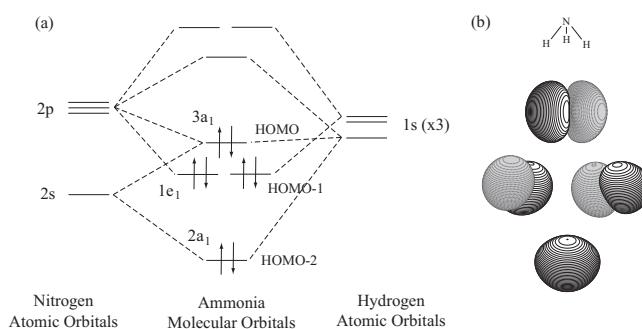


FIG. 1. (a) Molecular orbital diagram of the valence orbitals of NH_3 . (b) Corresponding spatial orbital representations generated with GAUSSIAN 03¹⁵ for the four valence orbitals. The diagram shows the $3a_1$ highest occupied molecular orbital is anti-bonding with p -like character. The $1e_1$ state is doubly degenerate, consisting of two molecular orbitals with p -like character. By contrast, the $2a_1$ HOMO-2 state has s -like character.

characteristics. The second energy level, or next highest occupied molecular orbital (NHOMO or HOMO-1) is a doubly degenerate bonding level with $1e_1$ symmetry. Again, this orbital is found to have significant p -like character from EMS measurements.¹⁷ The third energy level, HOMO-2, is a singly degenerate bonding orbital, and has s -like character in contrast to the outer orbitals.

While these characteristics and symmetry labels are derived from simple molecular orbital theory, they can be helpful in interpreting the data and are important in the calculations. The different characteristics of the orbitals have a significant effect when averaging the target wavefunctions over all possible orientations prior to the collision, since parity inversion of p -character states would largely cancel contributions to the scattering process unless carefully considered. By contrast, wavefunctions of s -character do not suffer from parity inversion, and so the orientation averaging of these wavefunctions is more straightforward. A fuller discussion of these effects and their consequences is presented in Sec. IV.

III. THE EXPERIMENTAL APPARATUS

The experimental data presented here were taken using the fully computer controlled and optimised ($e,2e$) spectrometer in Manchester. This spectrometer is described in Ref. 18 and so only the pertinent details are given here. The spectrometer can operate over a range of geometries from a coplanar geometry, where the incident electron is in the same plane as the two outgoing electrons ($\psi = 0^\circ$), to the perpendicular geometry, where the incident electron is orthogonal to the detection plane ($\psi = 90^\circ$) (see Figure 2).

The incident electron beam was produced by a two-stage electron gun that had an energy resolution ~ 0.6 eV. The electron analyzers were mounted on individual turntables that enabled them to rotate independently around the detection plane. The experiments described here used a *doubly symmetric* geometry with $E_1 = E_2 = E$ and $\xi_1 = \xi_2 = \xi$ (see Figure 2). The TDCS was obtained by measuring the ionization probability for a range of angles ξ for a given energy E . Data in the perpendicular plane are presented in terms of the mutual

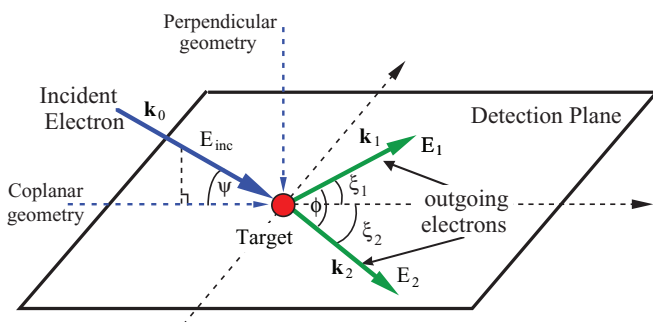


FIG. 2. Schematic diagram of the scattering geometry. A coplanar geometry is defined when the momenta of the incident and scattered electrons lie in the detection plane ($\psi = 0^\circ$). The analyzer angles ξ_1 and ξ_2 are measured with respect to the projection of the incident electron momentum in this plane. A perpendicular geometry is defined when the incident electron momentum is orthogonal to the detection plane ($\psi = 90^\circ$).

angle $\phi = \xi_1 + \xi_2$ since this is the only relevant angle in this geometry.

The ammonia target gas was admitted into the interaction region via a gas jet. The flow of ammonia was regulated by a needle valve so that the vacuum in the chamber was raised from a base pressure of $\sim 6 \times 10^{-7}$ Torr to 2.2×10^{-5} Torr. An incident electron beam current of 120 nA was used for measurements from the $3a_1$ and $1e_1$ orbitals and this was reduced to 50 nA when collecting data from the $2a_1$ state. These low beam currents were particularly important for the $2a_1$ state, due to the small cross-section from this orbital. This allowed acceptable accumulation rates to be delivered while maintaining good signal to background ratios.

The electrostatic focussing lenses in the analyzers were optimised under computer control, so as to allow for any small misalignment as they rotated around the detection plane. The energy of the spectrometer was calibrated at the start of each new experiment by tuning the incident electron energy to the peak in the coincidence binding energy spectrum. The three valence orbitals of ammonia are energetically well separated (11, 16.74, and 27.74 eV, respectively)¹⁰ and so were easily resolved within the energy resolution of the spectrometer (~ 1.4 eV in these experiments). As such, the measured TDCS was uncontaminated by contributions from neighbouring orbitals.

The data presented here have been individually scaled to unity at the highest point in the cross section, since absolute measurements were not obtained. Each dataset was generated from an average of several sweeps of the analyzers around the detection plane. The uncertainty in the TDCS as presented here is then the standard error derived from this averaging process. Angular uncertainties are due to the pencil angle of the incident electron beam and acceptance angle of the analyzers. This was estimated to be $\sim \pm 3^\circ$.

IV. THEORETICAL FRAMEWORK

The M3DW approximation has been presented in previous publications^{7,19,20} so only a brief outline of the theory will be presented. The TDCS for the M3DW is given by

$$\frac{d\sigma}{d\Omega_a d\Omega_b dE_b} = \frac{1}{(2\pi)^5} \frac{k_a k_b}{k_i} \times (|T_{dir}|^2 + |T_{exc}|^2 + |T_{dir} - T_{exc}|^2), \quad (1)$$

where \vec{k}_i , \vec{k}_a , and \vec{k}_b are the wave vectors for the initial, scattered, and ejected electrons, T_{dir} is the direct scattering amplitude, and T_{exc} is the exchange amplitude. The direct scattering amplitude is given by

$$T_{dir} = \langle \chi_a^-(\vec{k}_a, \mathbf{r}_1) \chi_b^-(\vec{k}_b, \mathbf{r}_2) C_{scat-eject}(r_{12}^{ave}) \times |V - U_i | \phi_{DY}^{OA}(\mathbf{r}_2) \chi_i^+(\vec{k}_i, \mathbf{r}_1) \rangle, \quad (2)$$

where r_1 and r_2 are the coordinates of the incident and the bound electrons, χ_i , χ_a , and χ_b are the distorted waves for the incident, scattered, and ejected electrons, respectively, and $\phi_{DY}^{OA}(r_2)$ is the initial bound-state Dyson molecular orbital averaged over all orientations. As mentioned in the Introduction, averaging states of odd parity would lose most of the information contained in the wavefunction due to cancellation.

Consequently, we average the absolute value of the wavefunction instead. Under the frozen orbital approximation, the Dyson orbital can be approximated using the initial bound Kohn-Sham orbital. The molecular wave functions were calculated using density functional theory (DFT) along with the standard hybrid B3LYP²¹ functional by means of the ADF 2007 (Amsterdam Density Functional) program²² with the TZ2P (triple-zeta with two polarization functions) Slater type basis sets.

The factor $C_{scat-eject}(r_{12}^{ave})$ is the Ward-Macek average Coulomb-distortion factor between the two final state electrons,²³ V is the initial state interaction potential between the incident electron and the neutral molecule, and U_i is a spherically symmetric distorting potential which is used to calculate the initial-state distorted wave for the incident electron $\chi_i^+(\vec{k}_i, \mathbf{r}_1)$.

Details about the calculation of initial and final state distorted waves can be found in Madison and Al-Hagan.²⁴ For the exchange amplitude T_{exc} , particles 1 and 2 are interchanged in the final state wavefunction in Eq. (2). However, for equal final state energies and angles, $T_{exc} = T_{dir}$ so it is not necessary to calculate both amplitudes.

We label results obtained from Eq. (2) as M3DW. Results will also be presented for Ne which are calculated similarly (using the same computer code) except that atomic wavefunctions and distorted waves are used. The atomic results are labeled 3DW. We will also show some results of the standard DWBA. The DWBA results are calculated identically to M3DW or 3DW except that the final state Coulomb interaction factor $C_{scat-eject}$ (normally called the post-collision interaction (PCI)) is not included in the evaluation of the T-matrix.

V. RESULTS AND DISCUSSION

Results are presented for a coplanar geometry in Sec. V A and for the perpendicular plane geometry in Sec. V B. As noted above, the three outermost orbitals were studied in a coplanar geometry, whereas data from only the two outermost orbitals were obtained in the perpendicular plane due to the very small cross sections in this plane. The results are also compared to data from the iso-electronic targets neon^{25,26} and methane,^{27,28} as were obtained previously in this spectrometer. This allows contrasts to be seen between targets that carry the same overall nuclear and electronic charge, but which have quite different structures.

A. Coplanar geometry

1. The HOMO $3a_1$ state

Experimental and theoretical TDCS for the $3a_1$ HOMO state of ammonia are presented in Figure 3 for six different energies ranging from $E = E_1 = E_2 = 20$ eV to 2.5 eV. The energy of the outgoing electrons is shown on individual plots. The ionization energy of this orbital is ~ 11 eV, and it has p -like character.

At the higher energies with outgoing electron energies $E = 20$ eV and 15 eV, the data are dominated by a large cross section in the forward scattering direction ($\xi < 90^\circ$) compared to that seen in the backward direction ($\xi > 90^\circ$). As the energy is lowered towards $E = 2.5$ eV the TDCS inverts to yield higher cross sections in the backward direction compared to forward scattering. The cross section in the backward direction is usually attributed to multiple scattering involving the

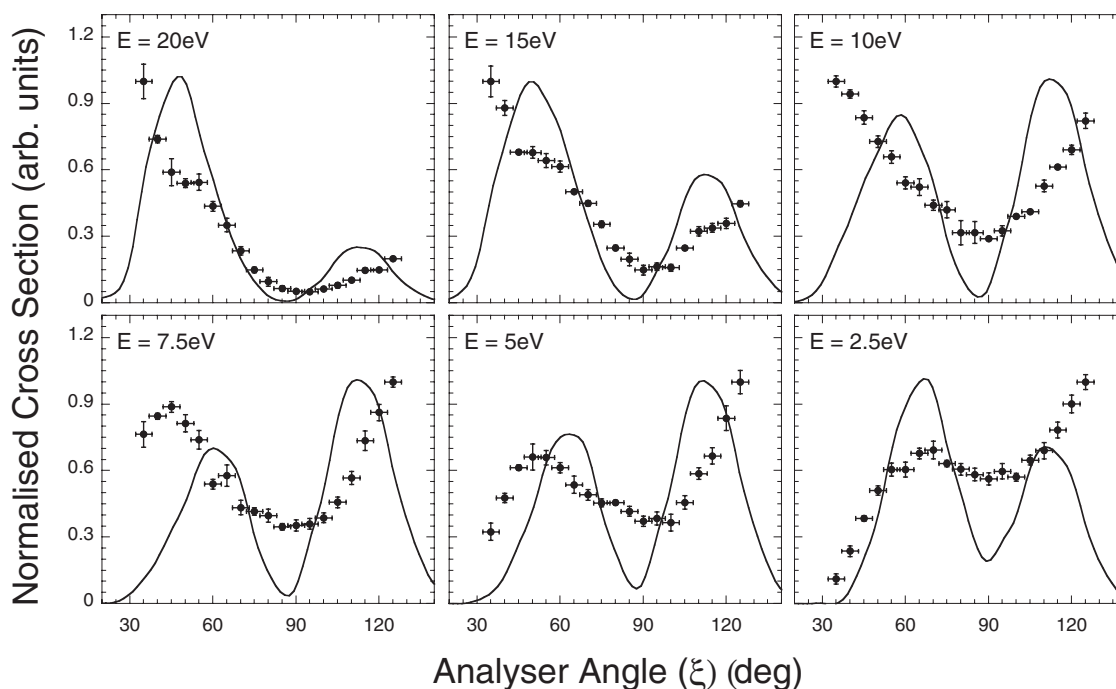


FIG. 3. TDCS from the $3a_1$ HOMO state of ammonia for coplanar symmetric kinematics. The energies of the outgoing electrons are shown in the respective plots. The experimental data (dots) and results from the molecular three-body distorted wave approximation (lines) are shown. The experimental and theoretical data have been independently normalised to unity at the peak for each energy.

nuclear core. This mechanism is more probable at lower energies since the electrons interact with the nucleus for a longer time, increasing the probability of the backward scattering, as is observed.

An additional effect normally observed in this energy regime is a migration of the forward peak towards $\xi = 90^\circ$ as the energy decreases. This angular shift occurs due to PCI between the outgoing electrons, brought about by their Coulomb repulsion. PCI plays an increasing role as the energy of the outgoing electrons is lowered, since they have more time to interact. PCI is also strongest when the outgoing electrons have equal energies, as in these measurements. The Coulomb repulsion between the electrons emerging from the interaction region effectively drives them apart, so that they emerge at a greater relative angle in the asymptotic region. This phenomenon is clearly observed in the data at the three lowest energies in Figure 3, with the peak moving from $\xi \sim 45^\circ$ for $E = 7.5$ eV to $\xi \sim 70^\circ$ for $E = 2.5$ eV. PCI should also cause the backward scattering peak to migrate towards $\xi = 90^\circ$. This latter movement cannot be verified in the current data, as the peak in this region is outside the range that can be measured.

An additional structure appears in the experimental data at the two highest energies, with the forward scattering peak exhibiting a shoulder in the cross section for $\xi \sim 50^\circ$. In atomic targets such as argon, “dips” are frequently found in the small angle peak which are attributed to the momentum probability of the p -like target orbital being zero at the origin.²⁹

Overall, the agreement between the experimental data and the theoretical prediction is fair, with most of the trends observed in the data also being reproduced by theory. The dominant forward and backward structures observed in the experiment are reproduced by theory, with the position of the minimum between the forward and backward peak being well represented. The forward peak movement towards $\xi = 90^\circ$ as the energy is lowered is also reproduced. The calculated

forward scattering peak is seen to steadily migrate from $\xi \sim 47^\circ$ to 67° as the outgoing electron energy is decreased from 20 eV to 2.5 eV. By contrast, theory predicts that the backward scattering peak should remain static at $\xi \sim 110^\circ$ for all these energies.

Despite the structural agreement between experiment and theory, the peak positions are not well reproduced. The position of the forward scattering peak is overestimated at all energies apart from at $E = 2.5$ eV, and the position of the backward peak is consistently underestimated for all energies. Theory also does not predict the shoulder in the forward scattering peak as is observed at higher energies. Except for $E = 2.5$ eV, theory does predict qualitatively the relative magnitudes of the forward and backward peaks with the forward peak becoming smaller and the backward peak growing with decreasing energy.

2. The $1e_1$ HOMO-1 state

The TDCS for the $1e_1$ HOMO-1 state are shown in Figure 4 at seven different energies. The $1e_1$ state has p -like character and is doubly degenerate, consisting of two bonding orbitals of equal energy (Figure 1). The ionization potential for this orbital is ~ 16.74 eV.

As for the $3a_1$ state, at higher energies the data show a large forward peak compared to backward scattering. The relative strength of the cross section in the backward direction increases as the energy is lowered, except for $E = 2.5$ eV. At high energies, the shoulder seen in the $3a_1$ data becomes more pronounced and becomes a “dip” at $\xi \sim 50^\circ$, for energies around $E = 10$ eV. As the energy decreases the forward peak again moves to higher angles; however, in this orbital the shift is larger with the peak being between $\xi = 70^\circ$ and 80° for energies from $E = 7.5$ eV to 2.5 eV. This shift in the peak position also effects the position of the minimum between

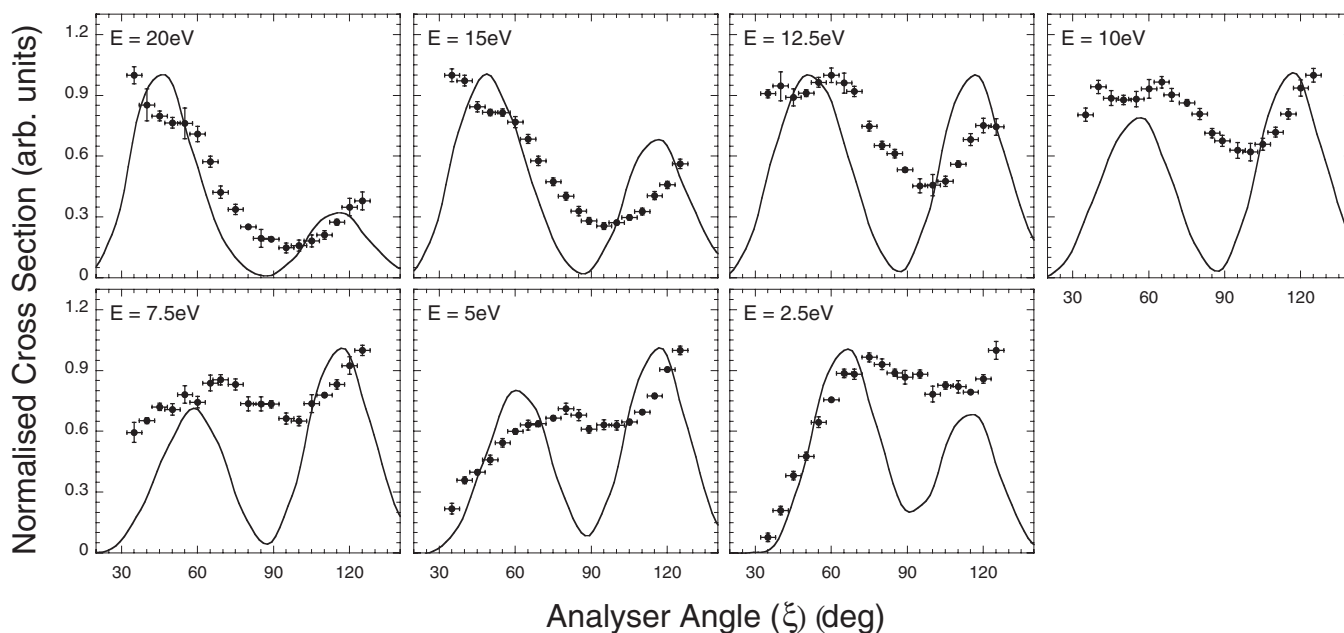


FIG. 4. As for Figure 3, for the $1e_1$ HOMO-1 state of NH_3 .

forward and backward peaks, which occurs at a higher angle in the $1e_1$ state compared to the $3a_1$ state. The minimum is significantly shallower in this orbital compared to the outermost orbital.

The theoretical calculations for the $3a_1$ HOMO and $1e_1$ HOMO-1 states are very similar. As a consequence, agreement between experiment and theory for the $1e_1$ state is less satisfactory than for the $3a_1$ state, since none of the differences between orbitals described above are reproduced by theory.

The calculation does predict a shift of the forward scattering peak towards $\xi = 90^\circ$ as the energy decreases, but does not accurately predict the magnitude of this shift. Theory, consequently, overestimates the position of the peak at high energies and underestimates the position at low energies. As for the outer orbital, the calculation consistently underestimates the position of the backward scattering peak. The position of the minima that was well reproduced for the $3a_1$ state is also underestimated for the $1e_1$ orbital. In both cases the magnitude of the minimum in the cross section is poorly reproduced. As with the $3a_1$, the calculation predicts that the relative intensity of the peak in the backward direction compared to the forward peak increases as the energy is lowered similar to the data, apart from at the lowest energy of $E = 2.5$ eV.

3. Comparison to iso-electronic targets CH_4 , NH_3 , and Ne with orbitals of p -character

Figure 5 shows representative TDCS data for the three iso-electronic targets CH_4 ,²⁷ NH_3 , and Ne,²⁵ with all orbitals having p -like character. For each target, data for outgoing electron energies of $E = 20$ eV and $E = 5$ eV are depicted. A similar trend in the TDCS is seen for the molecular

targets; however, neon shows quite different structures at both energies. At $E = 20$ eV the neon cross section exhibits a small third peak at $\xi \sim 85^\circ$, with two local minima at $\xi \sim 70^\circ$ and $\xi \sim 105^\circ$. The forward cross section clearly peaks at $\xi \sim 35^\circ$ and does not show the “dip” structure seen for the molecular targets as has been observed in neon at much higher energies.²⁵ The data from CH_4 at this energy show a “dip” in the cross section in the forward direction which is more pronounced than the NH_3 structure and occurs at a lower scattering angle. The ratio of forward to backward cross sections in both CH_4 and NH_3 is similar across all three orbitals.

At low energies the neon cross section does not show increased intensity in the backward direction, but is dominated by a forward peak at $\xi = 65^\circ$. A small structure is seen at $\xi \sim 95^\circ$ which may be the evolution of the central peak at $\xi \sim 85^\circ$ seen at the higher energy; however, the cross section at higher scattering angles monotonically decreases beyond this point. The structure of the cross section in neon is unusual, as most other targets show a greater intensity in the backward region compared to forward scattering at these low energies,²⁵ and as is predicted by the 3DW theory.

The data shown in Figure 5 indicate that the molecular nature of the targets plays a significant role in the scattering kinematics. It also appears that the different geometries of CH_4 and NH_3 do not impact greatly under these kinematic conditions. This is perhaps not surprising as the change in bond length and bond angle is relatively small between CH_4 and NH_3 , as is the change in nuclear charge of the central atom. Comparison between experiment and theory for neon in Figure 5 shows reasonable agreement at the higher energy with the calculation accurately predicting the forward scattering peak, and also predicting a small peak at $\xi \sim 85^\circ$. By contrast, the theoretical prediction at the low energy displays

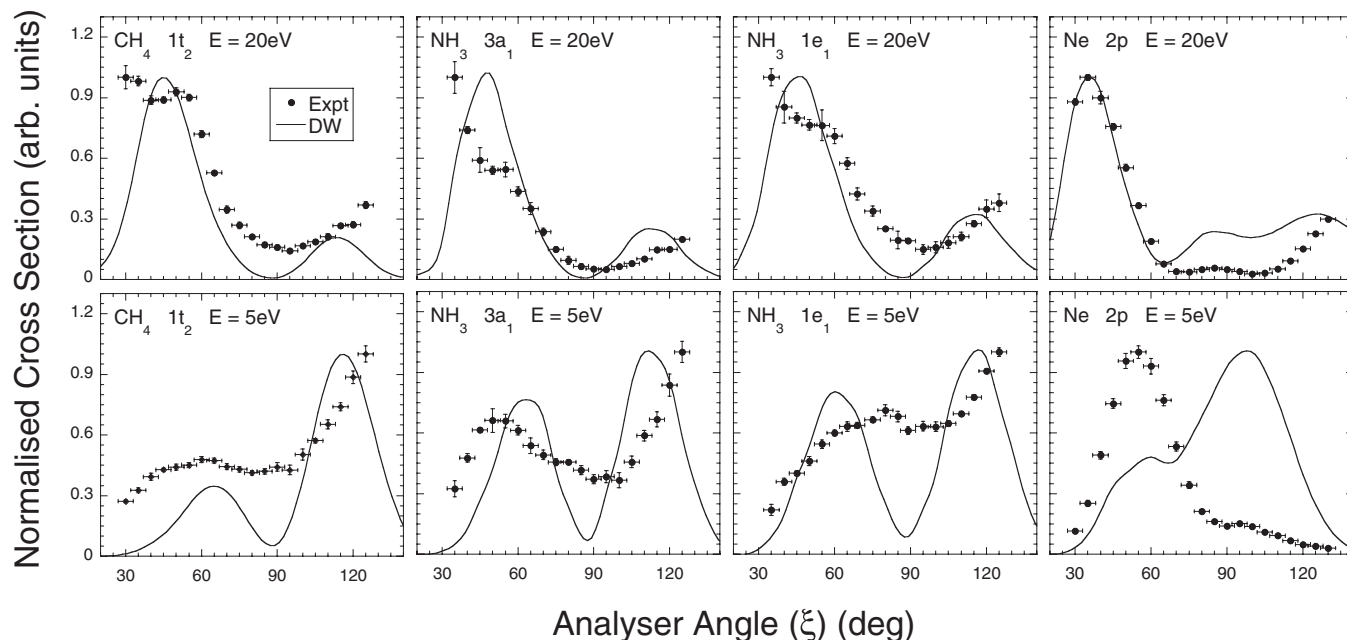
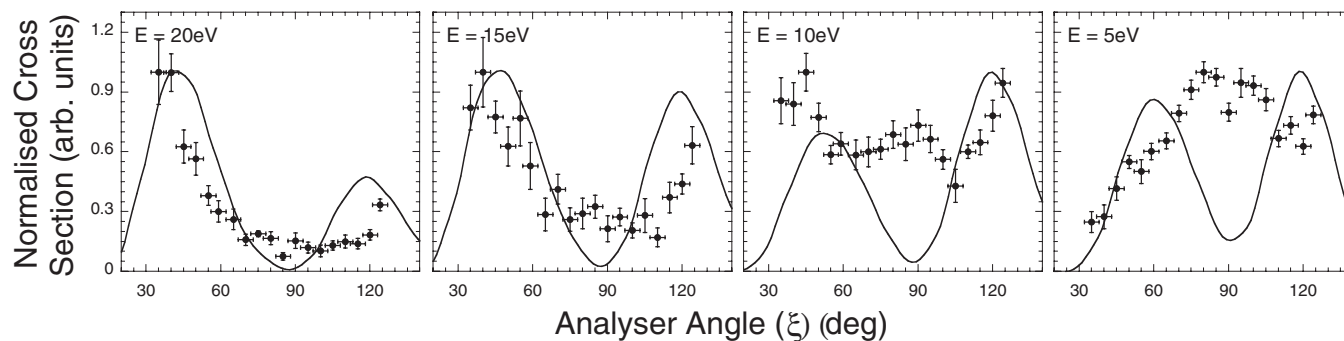


FIG. 5. TDCS for orbitals with p -like character from the iso-electronic series CH_4 ,²⁷ NH_3 , and Ne.²⁵ For each target results for two energies are given: the top row gives data for outgoing electron energies of 20 eV, while the bottom row shows data with outgoing energies of 5 eV. At left is the TDCS for the $1t_2$ HOMO state of CH_4 , the middle columns show results from the $3a_1$ and $1e_1$ states of NH_3 , and the right column gives data from the $2p$ state of Ne. The experimental data are compared to distorted wave theoretical predictions; M3DW for the molecular targets and 3DW for the atomic target.

FIG. 6. As for Figure 2, for the $2a_1$ state of NH_3 .

the trend of increased intensity in the backward region, but is opposite to the experimental data. It is surprising that the theory agrees better with experiment for low energy molecular targets than atomic targets since fewer approximations are made in the calculation for atomic targets.

Xu *et al.*¹³ recently suggested that the dip in the cross section seen at forward angles may be related to a nuclear scattering phenomenon, rather than simply being due to the p -like character of the orbital. However, since this dip is seen for all p -like orbitals in methane and ammonia as shown above, and yet is absent in the corresponding s -like orbitals in these targets (see Figure 7), it would appear that the underlying physical phenomena giving rise to the dip needs further investigation.

4. Ionization from the $2a_1$ state

The third orbital studied here is the $2a_1$ state, which has s -like character. Calculations for this orbital are expected to be more accurate, since uncertainties introduced through the

orientation averaging process should be largely eliminated for s -states, since they have approximately spherical electron distributions, and since their wavefunctions do not change under parity inversion. This expectation was contradicted in the study of methane²⁷ however, where the outermost p -character orbital gave better agreement between experiment and theory than the HOMO-1 state, which has s -character.

Figure 6 shows the new results for the HOMO-2 ($2a_1$ state) in NH_3 . The data show significantly more scatter than for the higher orbitals due to the lower cross section. At the higher energies a similar cross section to that for the outermost orbitals is observed. Once again, a higher intensity is seen for forward scattering compared to the backscatter region, with the peaks separated by a minimum at $\xi \sim 90^\circ$. The forward scattering peak shows no evidence of the structure seen for the HOMO and HOMO-1 states. As the energy is lowered, an additional peak emerges around $\xi = 90^\circ$, which is most evident at $E = 10$ eV. A three-peak structure is also observed for the iso-electronic targets neon²⁵ and CH_4 ²⁷ at this energy (see Figure 7). This middle peak emerges from the

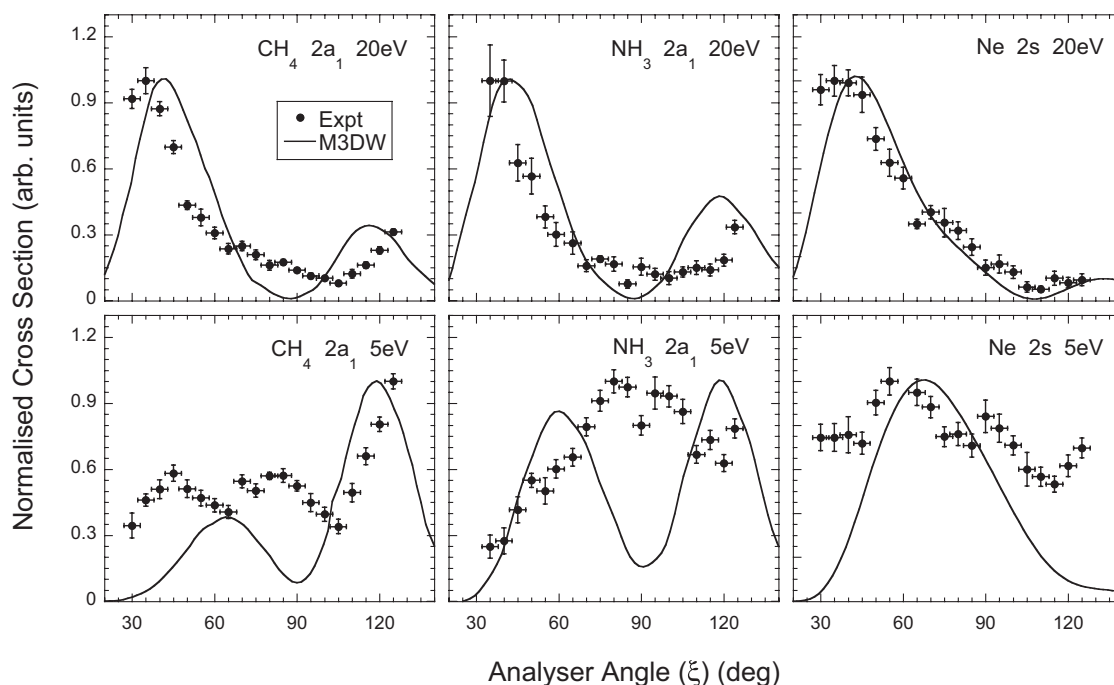


FIG. 7. TDCS for orbitals of s -like character for the three iso-electronic targets using different outgoing electron energies. The left plots are from the $2a_1$ (HOMO-1) of CH_4 ,²⁷ the $2a_1$ (HOMO-2) for NH_3 is shown in the central plots, and the $2s$ orbital of neon²⁵ is shown in the right-hand plots. The energies in each case are shown in the respective plots.

background as the energy is lowered, and is not due to a migration of either the forward or backward scattering peaks, as might be caused by PCI. In the previous study of methane,²⁷ this peak was attributed to a new scattering mechanism.

The calculated cross sections are similar in shape to that of the two outermost orbitals. At high energy, theory predicts atomic-like behaviour with a high forward scattering peak, a small backward peak, and a deep minimum in between similar to the data. The model again predicts that the relative intensity of the backward peak increases with decreasing energy, the minimum between the peaks shifting slightly in angle and increasing slightly in relative intensity. Experiment and theory are in better agreement for the two highest energies than was found for the two outermost orbitals. However, as for the two outermost orbitals, the calculation overestimates the position of the forward peak and underestimates that of the backward scattering peak. At lower energies, theory fails to predict the increasing intensity of the cross section in the middle region around $\xi = 90^\circ$ and does not predict the third peak that is observed. At the lowest energy of $E = 5$ eV the data show a maximum where theory predicts a minimum.

5. Comparison between orbitals of *s*-character in the iso-electronic targets

Figure 7 shows representative TDCS data for the three iso-electronic targets CH₄,²⁷ NH₃, and Ne,²⁵ with all orbitals having *s*-like character. For each target, data for outgoing electron energies of $E = 20$ eV and $E = 5$ eV are depicted. The data shown in Figure 7 indicate that scattering from *s*-like orbitals under these kinematic conditions is similar at $E = 20$ eV, irrespective of the iso-electronic target and energy. At $E = 5$ eV the cross sections for CH₄ and Ne both show a triple peak structure while that of NH₃ is dominated by a central peak at $\xi = 90^\circ$. Note that NH₃ also gives a triple peak structure at $E = 10$ eV. For all targets with *s*-like character, the theoretical calculation for $E = 20$ eV shows reasonable agreement with the data. By contrast, at the lower energies little agreement is found. This may be in part due to the low energies that are used, since distorted wave theories typically have difficulty modelling the collision in this low energy regime.

B. Scattering into the perpendicular plane

The experimental apparatus in Manchester has the capability to measure the ionization cross section over a wide range of geometries, as shown in Figure 2. The perpendicular plane ($\psi = 90^\circ$) was hence selected to further this study, since scattering into this plane requires a strong interaction to occur between the incident electron and the target nuclei.^{26,30} As such, scattering into this geometry maximises the sensitivity to these nuclear interactions. Further, only the mutual angle between the outgoing electrons $\phi = \xi_1 + \xi_2$ has meaning in this plane, due to rotational symmetry around the incident electron beam direction.

Data from the two outermost orbitals of NH₃ are presented below. No results from the $2a_1$ HOMO-2 state were obtained due to the very low scattering cross section into the

perpendicular plane for this orbital. The data are compared to DWBA and M3DW models over a range of energies from $E = 20$ eV to $E = 1.5$ eV, and are also compared to data from the iso-electronic targets CH₄²⁸ and Ne²⁶ in this energy regime.

1. Ionization from the $3a_1$ state in the perpendicular plane

Figure 8 shows data in the perpendicular plane for the HOMO $3a_1$ state of NH₃ at six energies from $E = 20$ eV to 1.5 eV. Predictions from the DWBA and M3DW that includes PCI are also shown for comparison.

At $E = 20$ eV the data show a two-peak symmetric structure with a deep minimum at $\phi = 180^\circ$, the peaks being located at $\phi = 90^\circ$ and $\phi = 270^\circ$. As the energy decreases, the position of the two peaks remains approximately constant; however, the local minimum at $\phi = 180^\circ$ becomes shallower. At $E = 10$ eV a small third peak at $\phi = 180^\circ$ appears, although this is difficult to see clearly. As the energy is lowered to $E = 5$ eV, the width of the distribution narrows and the cross section remains flat over a wide range of angles between the edges of the distribution. At still lower energies the cross section evolves into a single distribution centred at $\phi = 180^\circ$. A similar single-peak structure is seen in this geometry for helium at low energies,³¹ and this has been attributed to the dominance of PCI between the outgoing electrons³² at these energies. It may be that PCI is also playing a significant role for the molecular target.

Both DWBA and M3DW calculations predict three well-resolved peaks as seen in Figure 8, in contrast to the data. Al-Hagan *et al.*³⁰ compared perpendicular plane cross sections for ionization of H₂ and He and they found two peaks for H₂ and three peaks for He. They showed that the two peaks near $\phi = 90^\circ$ and $\phi = 270^\circ$ resulted from elastic scattering in the perpendicular plane for both H₂ and He and that the third peak at $\phi = 180^\circ$ resulted from backscattering from the central nucleus for He with no peak for H₂ due to the fact that there was no nucleus at the CM. Further they predicted that one should always find three peaks for molecules that had a nucleus at the CM and two peaks for molecules that did not have a nucleus at the CM. Although there is no nucleus at the CM for NH₃, the nitrogen nucleus is close enough to the CM that one might expect three peaks as predicted. Interestingly, theory predicts the three peaks while the experiment only has two for the higher energies.

The DWBA theory predicts a small, unphysical intensity at $\phi = 0^\circ$ and $\phi = 360^\circ$ since PCI is not included. At the higher energies the DWBA predicts two dominant peaks at $\phi = 90^\circ$ and $\phi = 270^\circ$ with a small central peak at $\phi = 180^\circ$. As the energy is lowered the calculated peaks remain in the same position and the small central peak increases in intensity. The M3DW model (which includes PCI) predicts the two outer peaks to be slightly closer together at $\phi \sim 100^\circ$ and $\phi \sim 260^\circ$ at the highest energy. As the energy decreases, the outer peaks move toward $\phi = 180^\circ$ and the intensity of the central feature increases until it becomes the dominant peak in qualitative agreement with experiment. Since the M3DW calculation includes PCI (in contrast to the DWBA model),

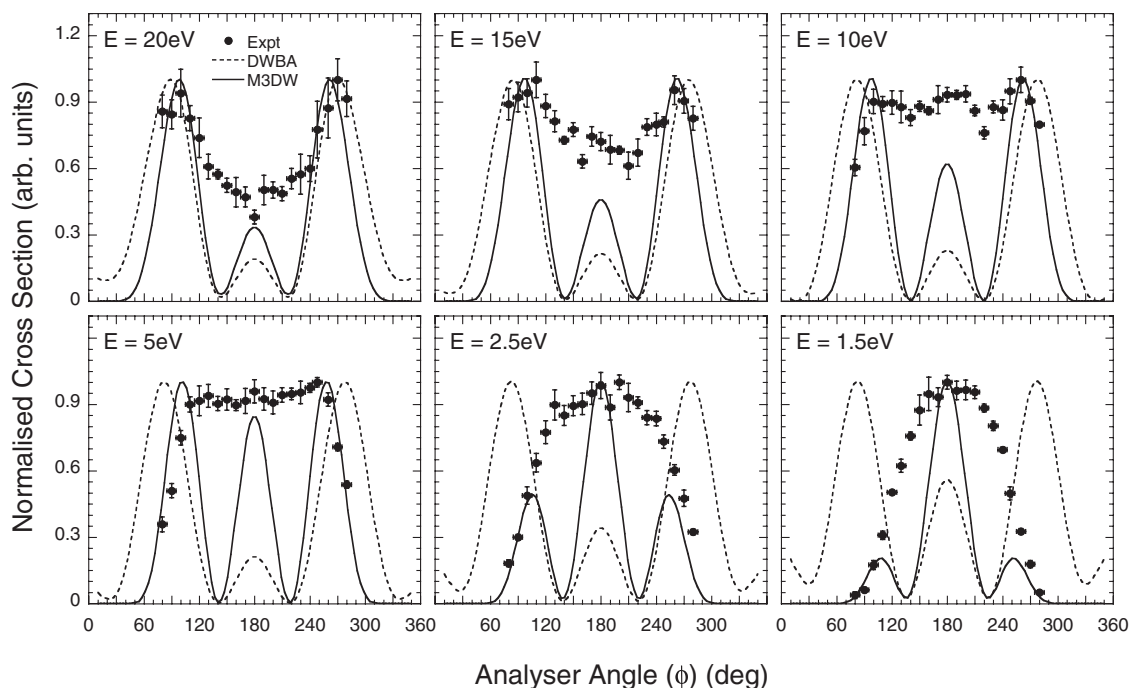


FIG. 8. TDCS from the $3a_1$ state (HOMO) of ammonia in perpendicular kinematics. The energies of the outgoing electrons are shown in the respective plots. The experimental data (dots) and prediction from a distorted wave Born approximation (dashed lines) and molecular three-body distorted wave approximation (solid lines) are shown. The data and theoretical curves have been independently normalised to unity at their peak for each energy.

it appears that PCI is making a significant contribution to the relative intensity of the central peak, and contributes to the shift in position of the outer peaks. The M3DW is in better agreement with the data in terms of the position of the outside peaks and width of the distribution.

2. Ionization from $1e_1$ state

Figure 9 presents the results from the $1e_1$ state, again at six energies from $E = 20$ eV to $E = 1.5$ eV. Once again the data and calculations are independently normalised to unity at the peak. The observations made for the $3a_1$ state are largely applicable to the data in Figure 9, as the results from both states are similar. This is consistent with the coplanar data, where orbitals of the same character produced similar cross sections. In the perpendicular plane experiments for the $1e_1$ state the highest energy was $E = 15$ eV, although the theoretical calculations extend to 20 eV. At $E = 15$ eV a twin-peak structure is again seen with a shallow minimum at $\phi = 180^\circ$. In contrast to measurements from the $3a_1$ state, the peaks in the $1e_1$ state data steadily move closer to $\phi = 180^\circ$ as the energy is reduced. At low energies the distribution has merged into a single peak at $\phi = 180^\circ$ as seen for the HOMO orbital.

The DWBA model once again predicts finite intensity at $\phi = 0^\circ$ and $\phi = 360^\circ$, since PCI is not included. The M3DW calculation is almost identical in shape for the $3a_1$ and $1e_1$ states. This model once again accurately models the overall width of the distribution; however, it fails to predict the structure in the data and shows three peaks at all energies, with a dominant central peak for lower energies.

3. Orbitals of p -like character in the iso-electronic targets (perpendicular plane geometry)

Figure 10 shows the TDCS in the perpendicular plane for CH_4 , NH_3 , and Ne for orbitals with p -like structure. Data at three different energies are shown for each target, from a high energy ($E = 20$ eV or 25 eV) down to low energy ($E = 2.5$ eV or 1.5 eV). A comparison between the outermost orbital cross sections in the perpendicular plane for Ne and CH_4 was presented in Nixon *et al.*²⁶ and so will not be repeated here. In brief, the data for neon are subtly different from that for CH_4 and are relatively well represented by the theory.

From Figure 10 it can be seen that similar results are obtained for all three p -like orbitals in CH_4 and NH_3 , while neon exhibits slightly different behaviour. The cross sections for neon do not evolve into a wide distribution with a relatively flat top as for the molecules, but rather show movement of the two peaks towards each other as the energy is lowered. At the lowest energy a single peak is again observed.

It is interesting to note for neon that the calculation which does not include PCI appears to fit the data well at both $E = 25$ eV and $E = 10$ eV in the region near $\phi = 180^\circ$ while overestimating the cross section for small and large angles where PCI is most important. Inclusion of PCI (solid line) yields qualitative agreement with the shape of the data for $E = 25$ eV and very good agreement with the data for the lowest energy $E = 2.5$ eV. As the energy is lowered, the two theoretical peaks including PCI merge to a single peak by $E = 10$ eV in contrast to experiment. PCI is clearly important for this target in this energy regime; however, it appears that the energetic effects of this interaction need to be more carefully considered. Overall, agreement between experiment and theory for neon is much better than for the molecular targets.

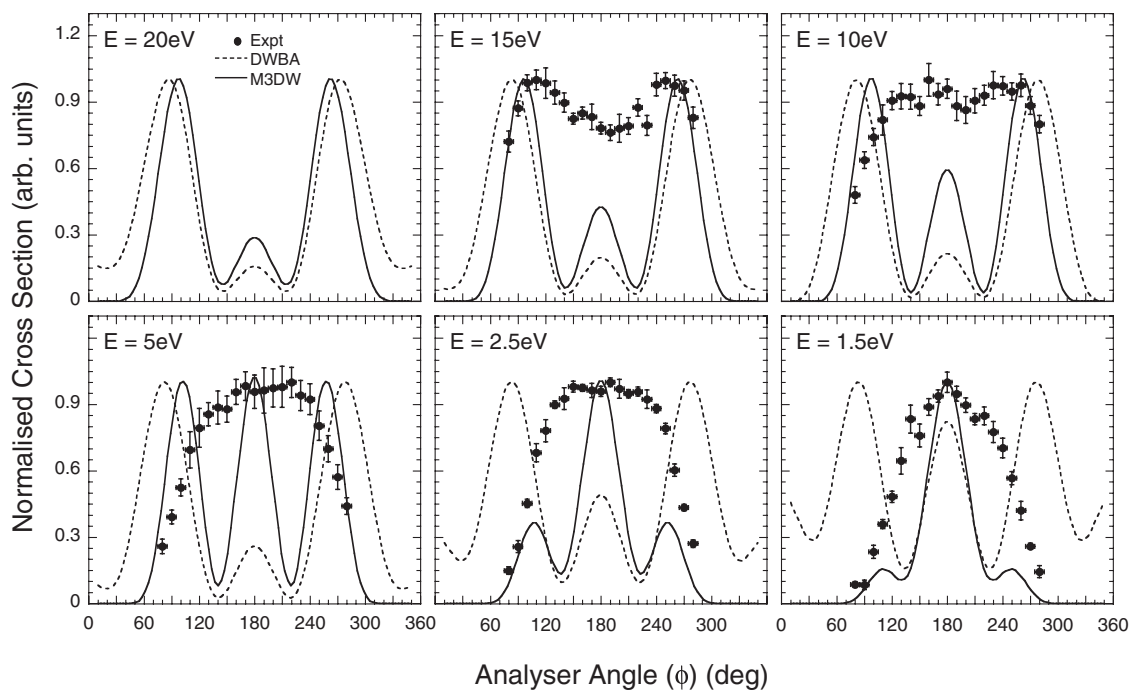
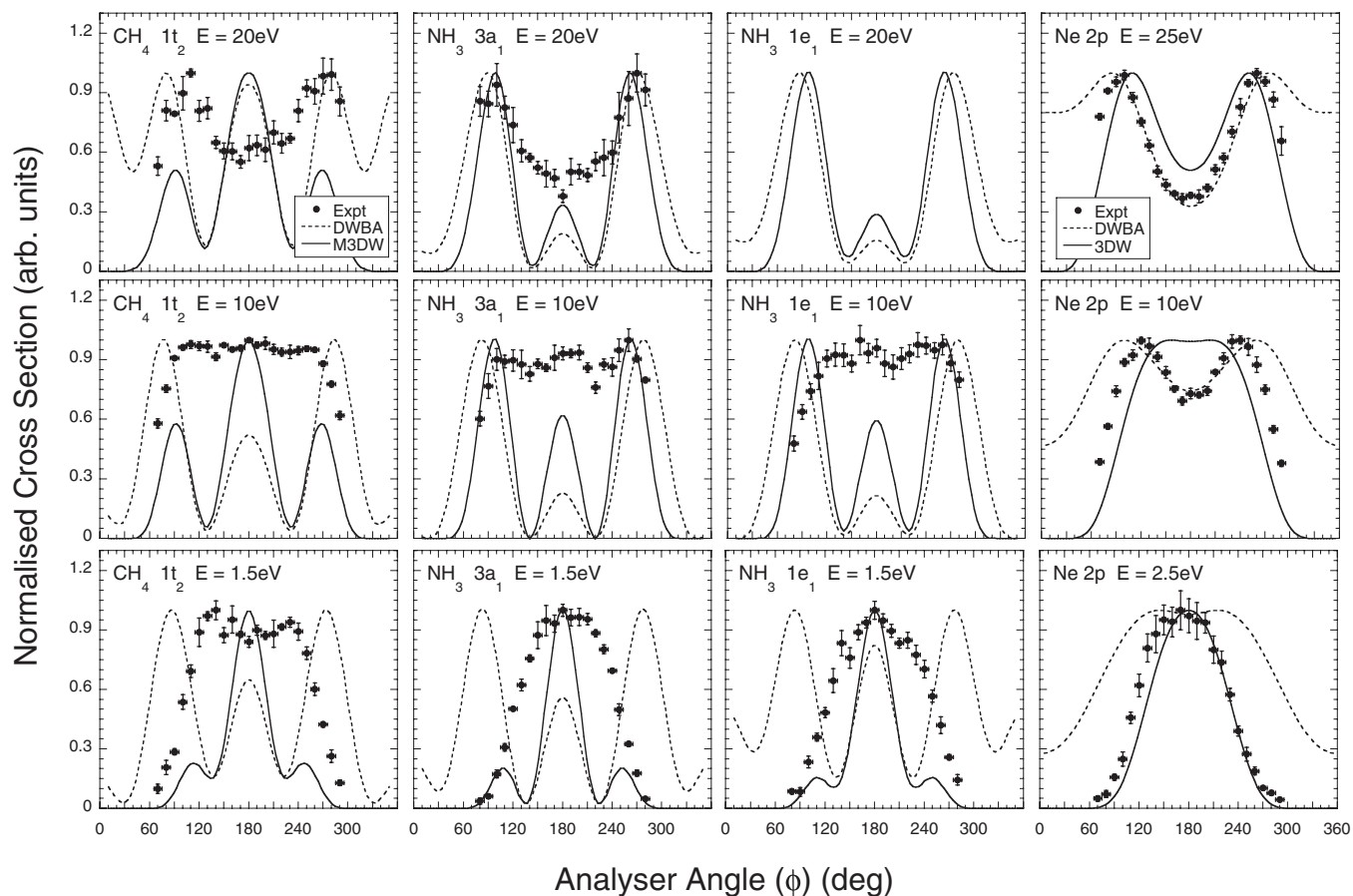
FIG. 9. As for Figure 8, for the $1e_1$ state (HOMO-1) of NH_3 .

FIG. 10. TDCS in the perpendicular plane for orbitals with p -like character for the iso-electronic series. The left hand panels show data for the HOMO orbital of CH_4 ,²⁸ the middle two columns show data for the HOMO and HOMO-1 orbitals of NH_3 , respectively, and the right hand column shows the data from Ne .²⁶ For each target three energy regimes are shown, labeled on the individual plots.

This suggests that in the perpendicular plane the treatment of the molecular nature of the target has a stronger influence on the level of agreement between the calculation and the data.

VI. CONCLUSIONS

Experimental ($e,2e$) data for the ionization of NH_3 have been presented for both coplanar and perpendicular plane geometries, and have been compared to predictions from distorted wave Born approximation and molecular three-body distorted wave calculations. The outer three orbitals of NH_3 were selected for this study. Agreement between experiment and theory is mixed. For the coplanar geometry some agreement is found at higher energies for all three orbitals; however, this is less satisfactory at lower energies. The $3a_1$ and $1e_1$ states both have p -like character and their measured cross sections are similar. The cross sections for ionization from these orbitals are similar to that of the outermost orbital of methane, which also has p -like character. Significant differences are found in the HOMO-2 orbital when compared with the outer orbitals. This is due to the different character of the orbital, which is s -like. Orbitals with s -like character in the iso-electronic targets neon and methane also show similar features to the data from the $2a_1$ orbital in ammonia. It appears that, in a coplanar geometry, the character of the orbitals plays a dominant role in describing the interaction, rather than the nuclear structure of the target.

In the perpendicular geometry a set of data is presented for the two outermost orbitals of NH_3 , which is again similar to the data from CH_4 . A closer agreement with experiment is found for the M3DW calculation than the DWBA calculation, due to the inclusion of PCI. However, in all of the iso-electronic species that have been investigated to date (neon,²⁶ ammonia, methane,²⁸ and water³³), theory predicts considerably more structure than is observed. It would again appear that the orbital symmetry is playing a dominant role in controlling the ionization cross section, compared to differences in the structure of the target.

These observations are not reflected in the calculations, since the structural predictions for all three orbitals in ammonia are remarkably similar. This would suggest that the models are at present dominated by the scattering dynamics from the nuclei, and not enough emphasis is being attributed to the electron distribution within the individual target orbital. This observation brings into question the accuracy of the OAMO (orientation averaged molecular orbital) approximation for these targets.

ACKNOWLEDGMENTS

K.L.N. would like to thank the Royal Society for a Newton International Fellowship at the University of Manchester. We would like to thank the technicians in the

Schuster laboratory for providing excellent support for the experimental apparatus. This work was partly supported by the US National Science Foundation under Grant No. PHY-1068237 and by the National Natural Science Foundation of China under Grant No. 11174175. Computational work was performed with Institutional Computing resources made available through Los Alamos National Laboratory.

- ¹I. E. McCarthy and E. Weigold, *Rep. Prog. Phys.* **54**, 789 (1991).
- ²A. Prideaux and D. H. Madison, *Phys. Rev. A* **67**, 052710 (2003).
- ³R. Srivastava, T. Zup, R. P. McEachran, and A. D. Stauffer, *J. Phys. B* **25**, 1073 (1992).
- ⁴M. S. Pindzola, F. Robicheaux, S. D. Loch, J. C. Berengut, T. Topcu, J. Colgan, M. Foster, D. C. Griffin, C. P. Ballance, D. R. Schultz, T. Minami, N. R. Badnell, M. C. Witthoef, D. R. Plante, D. M. Mitnik, J. A. Ludlow, and U. Kleiman, *J. Phys. B* **40**, R39 (2007).
- ⁵I. Bray and A. T. Stelbovics, *Phys. Rev. Lett.* **69**, 53 (1992).
- ⁶O. Zatsarinny and K. Bartschat, *Phys. Rev. A* **85**, 062710 (2012).
- ⁷J. Gao, D. H. Madison, and P. L. Peacher, *J. Chem. Phys.* **123**, 204302 (2005).
- ⁸C. Champion, C. Dal Capello, S. Houamer, and A. Mansouri, *Phys. Rev. A* **73**, 012717 (2006).
- ⁹I. Toth and L. Nagy, *J. Phys. B* **43**, 135204 (2010).
- ¹⁰M. S. Banna and D. A. Shirley, *J. Chem. Phys.* **63**, 4759 (1975).
- ¹¹J. S. Zhu, Y. R. Miao, J. K. Deng, and C. G. Ning, *J. Chem. Phys.* **137**, 174305 (2012).
- ¹²Z. Rezkallah, S. Houamer, C. Dal Capello, I. Charpentier, and A. C. Roy, *Nucl. Instrum. Methods Phys. Res. B* **269**, 2750 (2011).
- ¹³S. Xu, H. Chaluvadi, X. Ren, T. Pfluger, C. G. Ning, S. Yan, P. Zhang, J. Yang, J. Ullrich, D. H. Madison, and A. Dorn, *J. Chem. Phys.* **137**, 024301 (2012).
- ¹⁴I. Toth and L. Nagy, *J. Phys. B* **44**, 195205 (2011).
- ¹⁵M. J. Frisch, G. W. Trucks, H. B. Schlegel *et al.*, GAUSSIAN 03, Gaussian, Inc., Wallingford, CT, 2004.
- ¹⁶P. Atkins and J. de Paula, *Atkins Physical Chemistry*, 9th ed. (Oxford University Press, 2010).
- ¹⁷A. O. Bawagan, R. Muller-Fiedler, C. R. Brion, E. R. Davidson, and C. Boyle, *Chem. Phys.* **120**, 335 (1988).
- ¹⁸A. J. Murray, B. C. H. Turton, and F. H. Read, *Rev. Sci. Instrum.* **63**, 3346 (1992).
- ¹⁹J. Gao, D. H. Madison, and J. L. Peacher, *J. Chem. Phys.* **123**, 204314 (2005).
- ²⁰J. Gao, D. H. Madison, and J. L. Peacher, *Phys. Rev. A* **72**, 032721 (2005).
- ²¹C. Lee, W. Yang, and R. G. Parr, *Phys. Rev. B* **37**, 785 (1988).
- ²²C. F. Guerra, J. G. Snijders, G. te Velde, and E. J. Baerends, *Theor. Chem. Acc.* **99**, 391 (1998).
- ²³S. J. Ward and J. H. Macek, *Phys. Rev. A* **49**, 1049 (1994).
- ²⁴D. H. Madison and O. Al-Hagan, *Journal of Atomic, Molecular and Optical Physics* **2010**, 367180 (2010).
- ²⁵K. L. Nixon and A. J. Murray, *Phys. Rev. A* **87**, 022712 (2013).
- ²⁶K. L. Nixon, A. J. Murray, and C. Kaiser, *J. Phys. B* **43**, 085202 (2010).
- ²⁷K. L. Nixon, A. J. Murray, H. Chaluvadi, C. Ning, and D. H. Madison, *J. Chem. Phys.* **134**, 174304 (2011).
- ²⁸K. L. Nixon, A. J. Murray, H. Chaluvadi, S. Amami, D. H. Madison, and C. Ning, *J. Chem. Phys.* **136**, 094302 (2012).
- ²⁹G. Stefani, R. Camilloni, and A. Giardini-Guidonu, *J. Phys. B* **12**, 2583 (1979).
- ³⁰O. Al-Hagan, C. Kaiser, D. H. Madison, and A. J. Murray, *Nat. Phys.* **5**, 59 (2009).
- ³¹A. J. Murray and F. H. Read, *Phys. Rev. A* **47**, 3724 (1993).
- ³²G. Wannier, *Phys. Rev.* **90**, 817 (1953).
- ³³K. L. Nixon, A. J. Murray, O. Al-Hagan, D. H. Madison, and C. G. Ning, *J. Phys. B* **43**, 035201 (2010).